Acta Biomaterialia 171 (2023) 155–165

Contents lists available at ScienceDirect

Acta Biomaterialia

journal homepage: www.elsevier.com/locate/actbio

Full length article

Untangling the mechanisms of pulmonary arterial hypertension-induced right ventricular stiffening in a large animal model

Sotirios Kakaletsis[a], Marcin Malinowski[b,c], J. Caleb Snider[d], Mrudang Mathur[e], Gabriella P. Sugerman[f], Jeffrey J. Luci[g,h], Colton J. Kostelnik[e,f], Tomasz Jazwiec[b,i], Matthew R. Bersi[d], Tomasz A. Timek[b], Manuel K. Rausch[a,e,f,*]

[a] Department of Aerospace Engineering & Engineering Mechanics, The University of Texas at Austin, Austin, TX, USA
[b] Division of Cardiothoracic Surgery, Spectrum Health, Grand Rapids, MI, USA
[c] Department of Cardiac Surgery, Medical University of Silesia, Katowice, Poland
[d] Department of Mechanical Engineering & Materials Science, Washington University at St. Louis, St. Louis, MO, USA
[e] Department of Mechanical Engineering, The University of Texas at Austin, TX, USA
[f] Department of Biomedical Engineering, The University of Texas at Austin, TX, USA
[g] Center for Advanced Human Brain Imaging Research, Rutgers University, Piscataway, NJ, USA
[h] Scully Neuroimaging Center, Princeton University, Princeton, NJ, USA
[i] Department of Cardiac, Vascular and Endovascular Surgery and Transplantology, Medical University of Silesia in Katowice, Silesian Centre for Heart Diseases, Zabrze, Poland

ARTICLE INFO

Article history:
Received 4 May 2023
Revised 20 September 2023
Accepted 26 September 2023
Available online 4 October 2023

Keywords:
Mechanical testing
Diffusion tensor imaging
Magnetic resonance imaging
Histology
Immunohistochemistry
Hypertrophy
Remodeling

ABSTRACT

Pulmonary hypertension (PHT) is a devastating disease with low survival rates. In PHT, chronic pressure overload leads to right ventricle (RV) stiffening; thus, impeding diastolic filling. Multiple mechanisms may contribute to RV stiffening, including wall thickening, microstructural disorganization, and myocardial stiffening. The relative importance of each mechanism is unclear. Our objective is to use a large animal model to untangle these mechanisms. Thus, we induced pulmonary arterial hypertension (PAH) in sheep via pulmonary artery banding. After eight weeks, the hearts underwent anatomic and diffusion tensor MRI to characterize wall thickening and microstructural disorganization. Additionally, myocardial samples underwent histological and gene expression analyses to quantify compositional changes and mechanical testing to quantify myocardial stiffening. Finally, we used finite element modeling to disentangle the relative importance of each stiffening mechanism. We found that the RVs of PAH animals thickened most at the base and the free wall and that PAH induced excessive collagen synthesis, increased cardiomyocyte cross-sectional area, and led to microstructural disorganization, consistent with increased expression of fibrotic genes. We also found that the myocardium itself stiffened significantly. Importantly, myocardial stiffening correlated significantly with collagen synthesis. Finally, our computational models predicted that myocardial stiffness contributes to RV stiffening significantly more than other mechanisms. Thus, myocardial stiffening may be the most important predictor for PAH progression. Given the correlation between myocardial stiffness and collagen synthesis, collagen-sensitive imaging modalities may be useful for estimating myocardial stiffness and predicting PAH outcomes.

Statement of significance

Ventricular stiffening is a significant contributor to pulmonary hypertension-induced right heart failure. However, the mechanisms that lead to ventricular stiffening are not fully understood. The novelty of our work lies in answering this question through the use of a large animal model in combination with

* Corresponding author at: The University of Texas at Austin, 2617 Wichita Street, Austin, TX 78712.
E-mail address: manuel.rausch@utexas.edu (M.K. Rausch).

https://doi.org/10.1016/j.actbio.2023.09.043

spatially- and directionally sensitive experimental techniques. We find that myocardial stiffness is the primary mechanism that leads to ventricular stiffening. Clinically, this knowledge may be used to improve diagnostic, prognostic, and therapeutic strategies for patients with pulmonary hypertension.

1. Introduction

Pulmonary hypertension (PHT) is a devastating disease with a survival rate of only 58 % at 3 years [1]. For those eventually succumbing to PHT, complications associated with right heart failure are the predominant cause of death [2,3]. When failing, the right heart can show hallmarks of both systolic and diastolic dysfunction [4]. Interestingly, recent evidence suggests that measures of diastolic dysfunction may be better predictors of adverse clinical outcomes [5]. That is, decreased compliance of the right ventricle (RV) – or, alternatively, increased stiffness of the RV – during diastolic filling has been shown to correlate strongly with PHT disease progression [6–8]. Clearly, understanding the geometric, structural, and biological factors that contribute to RV stiffening is of significant clinical interest.

The proposed mechanisms driving RV stiffening and impaired diastolic filling range from the molecular to the organ scale. In particular, it has been proposed that three distinct mechanisms are responsible for RV stiffening: i) RV thickening, leading to structural resistance to filling, ii) extracellular matrix remodeling, leading to a less organized myocardium, iii) and myocardial remodeling via intracellular and extracellular mechanisms. The latter leads to stiffening of the myocardium itself, independent of thickening and microstructural disorganization [8–11]. The relative onset of each mechanism may vary and depend on the disease severity [8]. That is, not all mechanisms have to be present at all times.

Interestingly, the relative contribution of each of these factors to global stiffening of the RV is unclear. Given the predictive power of RV stiffening for PHT outcomes, disentangling the different mechanisms of PHT-induced RV stiffening could reveal novel treatment targets, identify new diagnostic markers, and improve prognosis. However, doing so is not without its challenges. Chief among them is that the proposed RV stiffening mechanisms may occur simultaneously; thereby, obfuscating their individual roles.

Additionally, given the limitations of non-invasive imaging techniques in right heart failure patients, most prior work has relied on non-mechanistic measures of stiffening, such as end-diastolic elastance [4]. In contrast, spatial and directional information could provide additional insight into mechanisms of RV diastolic dysfunction but has largely been ignored. Noteworthy exceptions are recent efforts toward image-based in-vivo RV strain measurements [12]. To overcome the limitations of non-invasive clinical assessment, the development of animal models has allowed for invasive measurements and therefore enabled the study of spatially- and directionally-sensitive properties of the RV [5,13,14]. However, most prior animal work has been limited to rodents and other small animal models where the relevance to the human condition is unclear [10,13,15–18].

Thus, the objective of our current work is to use a spatially- and directionally-sensitive repertoire of imaging, experimental, and computational modeling techniques to determine the relative contributions of wall thickening, microstructural disorganization, and myocardial stiffness to RV stiffening. Overall, our goal is to improve our understanding of the mechanisms contributing to PHT-induced RV stiffening with the hope of benefitting clinical practice and right heart failure patient outcomes.

2. Methods

2.1. Animal procedures

All animal procedures complied with the Principles of Laboratory Animal Care by the National Society for Medical Research. Moreover, all associated protocols abided by the Guide for Care and Use of Laboratory Animals by the National Academy of Science and were approved by the local Institutional Animal Care and Use Committee at Spectrum Health, MI.

In total, our study included twenty male Dorsett sheep (10–12 months of age, Hunter Dorsett Sheep, Lafayette, IN). Eight sheep underwent pulmonary artery banding to induce pulmonary arterial hypertension (PAH group, $n = 8$), while the remaining animals served as controls and did not undergo pulmonary artery banding (CTL group, $n = 12$). For pulmonary artery banding, we closely followed the procedure as reported by Verbelen et al. [19]. In short, we anesthetized the animals before accessing the pulmonary artery via a left thoracotomy through the 4th intercostal space. Next, we performed epicardial ultrasound to assess biventricular function as well as tricuspid and mitral valvular competence. We then encircled the pulmonary artery with an umbilical tape before its bifurcation. While monitoring systemic and pulmonary pressures via pressure catheters (PA4.5-X6; Konigsberg Instruments, Inc.), we tightened the tape progressively to the brink of hemodynamic instability. After a short observational period, we closed the chest and let the animals recover from the surgery.

After eight weeks of PAH disease progression, we anesthetized the animals, performed a sternotomy and conducted repeated epicardial ultrasound to assess biventricular and heart valve function. Without arresting the heart, we surgically placed a total of 14 sonomicrometry crystals (Sonometrics, London, Canada) across the RV free wall. At the same time, pressure catheters were placed in the right atrium as well as the left and right ventricles. Under open-chest conditions, we recorded sonomicrometry crystal positions as well as atrial and ventricular pressures for at least 10 cardiac cycles. At the end of the procedure, animals were euthanized, and we excised their hearts for downstream imaging and analysis. Control animals underwent the same terminal procedure.

Immediately after excision, we replaced the 14 epicardial sonomicrometry crystals with magnetic resonance imaging (MRI) visible markers (MR-spots, Beekley Corporation, Bristol, CT). The freshly excised hearts were then submerged in phosphate-buffered saline supplemented with the myosin inhibitor 2,3-Butanedione monoxime (Sigma Aldrich) to reduce myocardial contraction [20]. Stored on ice, we shipped the hearts overnight from Michigan to the University of Texas at Austin.

2.2. Magnetic resonance imaging

Upon receipt (approximately 12 h after euthanasia), we performed detailed MRI scans of each of the excised hearts. To this end, we first replaced the physiological solution with chilled perfluoropolyether oil (Fomblin 25/6, Solvay Solexis, Thorofare, NJ). Next, we placed the hearts in a 32-channel head/neck receiver coil (Siemens Healthineers, Erlangen, Germany), and scanned them in a Siemens Skyra 3.0 T human MRI scanner using a T_1-weighted

protocol and a Diffusion Tensor Imaging (DTI) protocol; additional details are provided in the supplement.

During postprocessing, we obtained the RV wall anatomy by segmenting the T_1-weighted anatomic MRI scans in the open-source software 3D Slicer (Version 4.11). Once segmented, we exported the segmented ventricles to MATLAB (Version R2021b) for RV wall volume and thickness calculations. Next, we converted the wall segmentation into an image mask, which we, in turn, imported into the open-source tractography software DSI Studio (June 16 2020, build) for analysis of DTI-MRI scans; more details are provided in the supplement. After conducting fiber tracking within the RV wall using DSI Studio, we exported the fiber tractography information into MATLAB for additional analysis. There, we subdivided the large RV fiber map into 14 myocardial regions as defined by the epicardial MR-spots. Next, we projected the 3D-fiber orientation vectors within each region onto four equidistant transmural planes between the epicardium and endocardium. We did so to match our histological data which we obtained across four transmural sections, see below. Finally, we fit the corresponding projected fiber vectors to a π-periodic von Mises distribution, viz.

$$R(\theta) = \frac{\exp\left(b\cos\left(2\left[\theta-\mu\right]\right)\right)}{2\pi I_o(b)} \quad (1)$$

where θ is the fiber direction, b is the concentration parameter, μ is the fiber mean angle, and I_o is the zeroth order Bessel function. Note that $b = 0$ represents a random fiber distribution, whereas $b \rightarrow inf$ represents a perfectly aligned fiber distribution.

2.3. Mechanical testing

Following completion of the MRI protocol, we rinsed the excised hearts and separated the RV wall from the remainder of the heart. Next, we excised myocardial cubes of approximately 10 mm edge size. Each sample was excised such that its edges aligned with the circumferential direction (C), the longitudinal direction (L), and radial direction (R). Then, we mounted these samples in our custom multi-axial shear tester, which we previously described in detail [20]. Once mounted, we deformed the samples in two simple shear modes up to 30 % strain and one tension-compression mode up to 10 % strain and recorded the force associated with each deformation. Then we removed the samples from the device, rotated the samples, re-mounted them, and repeated the next two shear modes and tension-compression mode until every unique orientation was tested. Together, our experiments yielded a total of six simple shear and three uniaxial tests per specimen. See Supplementary Figure S1 for a detailed depiction of each deformation mode.

To quantify the passive stiffness of each specimen, we transformed the force-displacement data into (Cauchy) stress-strain data and quantified stiffness as the slope of the stress-strain curves. To this end, we distinguished between two regimes: i) the low strain regime (i.e., toe stiffness) and ii) the high strain regime (i.e., calf stiffness).

2.4. Histology

After mechanical testing, we fixed samples in 10 % neutral-buffered formalin before submitting them to a commercial histology service for sectioning, staining, and imaging (Histoserv, Germantown, MD). Histoserv paraffin embedded and sectioned the samples before staining and imaging four equidistant, transmural slices with Masson's Trichrome. Upon receiving the slide images, we identified the relative fraction of collagen by conducting color thresholding as previously described [21,22]. Thresholding was conducted blinded to avoid bias.

2.5. Immunohistochemistry

A subset of mechanically tested, formalin-fixed samples were embedded and frozen in O.C.T. Compound (23-730-571, Fisher Scientific) prior to cryosectioning at a thickness of 8 µm. Cryosections were oriented transversely across the short axis of RV cardiomyocytes. After sectioning, O.C.T. compound was removed by a 5 min wash in phosphate buffered saline (PBS; without calcium and magnesium) at room temperature. Samples were incubated in 10 µg/mL wheat-germ agglutinin (WGA) conjugated to Alexa Fluor 488 (W11261, ThermoFisher Scientific) for 30 min at room temperature to label the cardiomyocyte cell membrane. Stained samples were washed in two 5 min exchanges of PBS then mounted in ProLong Gold Antifade with DAPI (P36935, ThermoFisher Scientific). Slides were imaged at 20x magnification on an Olympus BX53 microscope with a DP80 camera. In each image, cardiomyocyte area was defined as the area within each cell of the network of WGA-stained cardiomyocyte membranes [23]. Images were analyzed using a semiautomatic detection and analysis program in MATLAB (Version R2021) that included a series of image enhancement, binarization, skeletonization, object detection, and shape measurement. Regions with low quality staining were excluded from the analysis; a minimum of 50 cardiomyocytes were analyzed per image and over 6500 individual cardiomyocytes were analyzed per group.

2.6. Quantitative polymerase chain reaction (qPCR)

After mechanical testing, a subset of isolated RV tissue was homogenized using the TissueLyser II system. Total RNA was isolated using the Qiagen RNeasy Mini Kit (74104, Qiagen) and cDNA was synthesized using the SuperScript IV VILO system (11766050, Invitrogen). Real-Time qPCR was performed using PowerTrack SYBR Green Master Mix (A46012, Invitrogen) in a QuantStudio 3 Real-Time PCR system. Forward and reverse primers for specific genes of interest were constructed for the sheep genome (*Ovis aries*) and are listed in Supplementary Table S2. Relative gene expression was calculated for each sample based on differences in cycle number from the housekeeping genes *GAPDH* and *HPRT1*. Data are presented as normalized relative gene expression, and fold changes between groups were computed from $2^{-\Delta Ct}$ values [24]. Statistical analysis was performed on ΔCt values.

2.7. Finite element modeling

We constructed a representative model of the RV by approximating the endocardium as an ellipsoid section that matched the average radial-to-longitudinal length ratio of our MRI-derived epicardial geometries. To create the RV volume, we extruded the endocardial surface using the average MRI-derived, spatially varying wall thickness values. We discretized this geometry with 20,986 tri-linear hexahedral elements using a three-field formulation as implemented in FEBio (www.febio.org) [25,26], see Supplementary Figure S2 for a mesh convergence study. To model the mechanical behavior of the myocardium, we chose an incompressible Fung-type material model, see more details in the supplement. The parameters and microstructural organization for the control case were based on our previous experimental work [20]. That is, we assumed that fiber distributions follow a π-periodic von Mises distribution with a concentration parameter of $b = 1.12$. Additionally, based on our prior work, we assumed that the mean fiber angle varies transmurally from $+22.9°$ to $-76.4°$ between the epicardium and the endocardium, respectively [20]. We constrained the free surfaces of the RV wall to remain within plane; thus, enforcing symmetry conditions. Finally, we simulated the passive filling of the right ventricle under quasi-static conditions by applying

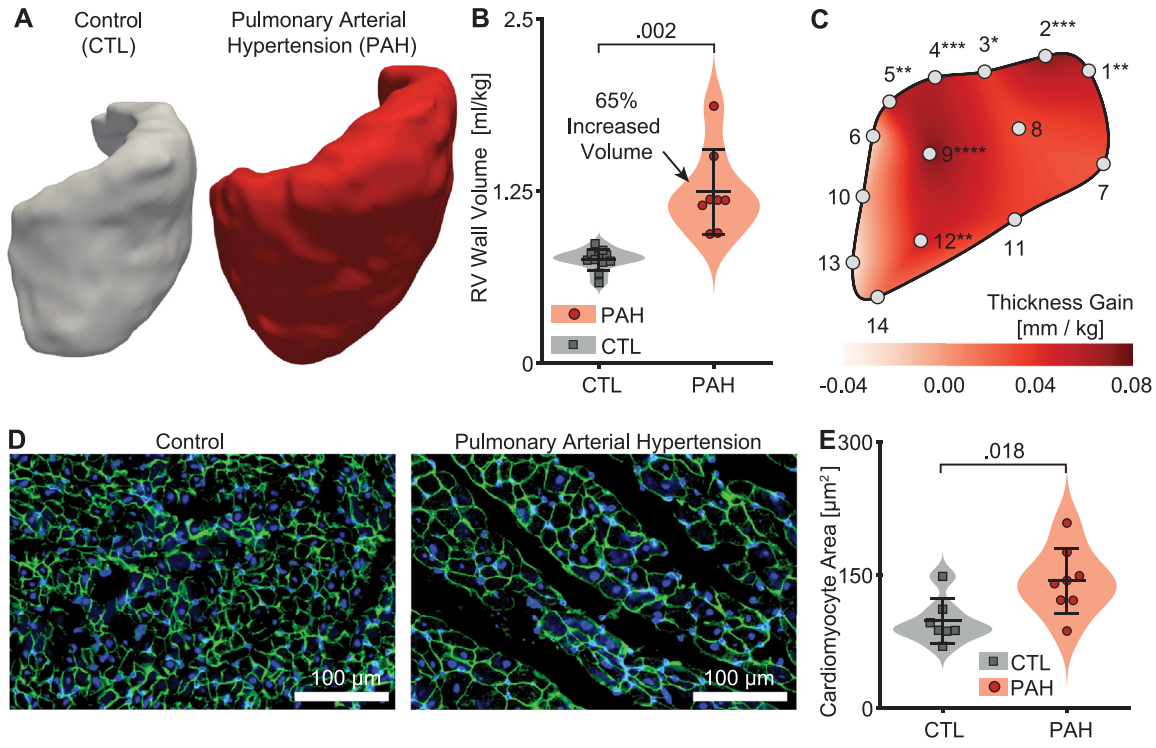

Fig. 1. Pulmonary arterial hypertension induced spatially-dependent RV thickening.
A) Representative right ventricular segmentations as measured via MRI. B) Pulmonary arterial hypertension (PAH) induced right ventricular volume increase as measured via MRI. C) Spatial map of the average local thickness increase computed by comparing the MRI-derived mean thickness maps between control (CTL, $n = 11$) and PAH ($n = 8$) animals (indexed by animal weight). Please note that discrepancies between subject numbers and specimen numbers stem from some hearts not having undergone MRI imaging. Base Markers: 1–5, Mid-wall Markers: 8,9,12, Septal Markers: 6,7,10,11,13, Apex Marker: 14. **** ($p < 0.0001$), *** ($p < 0.001$), ** ($p < 0.01$), * ($p < 0.05$). D) Representative Wheat Germ Agglutinin (WGA) stains of RV myocardium samples from CTL and PAH animals. E) PAH ($n = 8$) induced an ~46 % increase in the cardiomyocyte area with respect to the CTL ($n = 7$) group; an average of 4–5 images were included per sample for a total of 6549 cells (CTL) and 10,052 cells (PAH) analyzed. Please note that discrepancies between subject numbers and specimen numbers stem from limited specimen availability, and thus, some animals are not represented in the WGA stains.

an inner pressure of 40 mmHg and using the implicit nonlinear finite element solver FEBio (Version 3.6.0). To disentangle the impact of the different PAH-induced stiffening mechanisms on the diastolic pressure-volume curve (i.e., the filling curve), we repeated our control simulations after individually altering i) wall thickness, ii) the concentration parameter, and iii) stiffness of our constitutive model. Specifically, we modified the wall thickness by the average PAH-induced change as shown in Fig. 1C, changed the concentration parameter from $b = 1.12$ to $b = 0.56$, and multiplied the stiffness parameters 'a' of our constitutive law by 1.79, according to the mean findings in our experiments. Finally, we repeated the simulation once more with all three effects combined.

2.8. Statistics

For statistical comparisons between two independent groups, we first tested for normality via the Shapiro-Wilk test. Where at least one group was not normally distributed, we conducted Mann-Whitney U tests. Otherwise, we conducted independent Student's t-tests. For comparisons where multiple samples per animal were available, i.e., with between and within effects, we used linear mixed models. For comparing mean fiber angles in DTI-MRI data, we used a circular mixed model [27,28]. For all numeric data, we report mean +/- 1 standard deviation when normally distributed or median +/- interquartile range when non-normally distributed. Finally, we used a p-value of 0.05 as our significance level for all inference tests. All descriptive and inference statistical analyses were conducted in MATLAB (Version R2021) except for the linear mixed model analysis, which we conducted in R (Version 2021.09.0).

3. Results

3.1. Pulmonary artery banding induced pulmonary arterial hypertension in sheep

Eight weeks of pulmonary artery banding induced significant PAH in sheep as seen in Table 1. That is, PAH animals showed increased RV pressure at both end-diastole (ED) and end-systole (ES), as well as increased RV volume (based on ultrasound measurements). The increased RV pressures occurred in the absence of elevated LV pressure or central venous pressure (CVP). Moreover, PAH animals presented with tricuspid regurgitation (TR), reduced RV ejection fraction (EF), reduced fractional area contraction (FAC), and lower tricuspid annular plane systolic excursion (TAPSE); thus, clearly demonstrating reduced RV function. Hemodynamic data and clinical signs were comparable to Stage II-III of the New York Heart Association (NYHA) heart failure classification.

3.2. Pulmonary arterial hypertension induced spatially-dependent wall thickening

Using anatomic MRI scans of isolated sheep hearts, we compared both the RV volume and RV wall thickness between PAH and CTL animals. Both metrics were indexed using the animals' total body weights. Fig. 1A shows representative segmentations of a PAH RV (shown in red) and CTL RV (shown in white). We found that PAH induced significant hypertrophy ($p = 0.002$), leading to an average 65 % increase in mean RV volume, see Fig. 1B. Additionally, using our MR spot identification, we found that the RV volume increase was spatially heterogeneous ($p < 0.0001$) and

Table 1
Comparison between measures and right ventricular size and function between the hypertension (PAH) and control (CTL) groups.

	Control (CTL)		Hypertension (PAH)		*p*-value
	Mean/Median	Std/IQR	Mean/Median	Std/IQR	
Weight (kg)	62	2.5	63	1.6	0.0816
HR (bpm)*	110	20	108*	29*	0.7898
RVP ES (mmHg)	21	5.0	32	14	**0.0285**
RVP ED (mmHg)	4	2.4	12	4.4	**<0.001**
RVP max (mmHg)	29	5.8	40	16	**0.0234**
CVP ED (mmHg)	9*	2.0*	10	1.9	0.3510
LVP ES (mmHg)	60	18	50	21	0.4133
LVP ED (mmHg)	10	4.7	11	5.0	0.7426
LVP max (mmHg)	95	9.6	90	20	0.1546
TR (-)	1*	0.0*	4*	0.5*	**<0.001**
RVV ES (ml)	3.9	0.60	19	7.1	**<0.001**
RVV ED (ml)*	13	4.2	30*	10*	**<0.001**
RV EF (%)	66	8.5	45	7.0	**<0.001**
RV FAC (%)	51	5.7	41	8.4	**0.0044**
TAPSE (mm)*	1.4	0.39	0.7*	0.11*	**<0.001**

* Indicates that these data were not normally distributed and are therefore described via their median and inter-quartile range (IQR). HR, heart rate; RVP, right ventricular pressure; LVP, left ventricular pressure; CVP, central venous pressure; ES, end-systole; ED, end-diastole; TR, tricuspid regurgitation grade; RVV, right ventricular volume; RV EF, right ventricular ejection fraction; RV FAC, right ventricular fractional area contraction; and TAPSE, tricuspid annular plane systolic excursion.

driven by wall thickening primarily at the RV base (markers 1–5; $p < 0.05$) and the RV free wall (markers 9, 12; $p < 0.01$), but not at the apex (markers 7, 11, 14) or the interventricular septum (markers 6, 10, 13), see Fig. 1C. Based on WGA stains of CTL and PAH RV myocardium samples, we found that PAH significantly increased cardiomyocyte cross-sectional area, see Fig. 1D and E. Fig. 1D shows representative WGA stains labeling cardiomyocyte membranes (green) and nuclei (blue) for both control and diseased tissues. On average, cardiomyocyte cross-sectional area was increased by 46 % ($p = 0.018$) as a consequence of PAH, see Fig. 1E.

3.3. Pulmonary arterial hypertension increased extracellular collagen deposition

Based on Masson's Trichrome staining of RV free wall samples, we computed collagen content as area fractions within each field of view. Fig. 2A shows representative histology images from a PAH animal and a CTL animal demonstrating fibrotic collagen deposition in the former. Note that we included four equidistant transmural sections for each sample in our analysis. We found a significant increase in collagen content ($p < 0.0001$) in each section, see Fig. 2B. In fact, we found mean increases of 241, 310, 279, and 322 % in the epicardial sections (A), mid-wall sections (B) and (C), and the endocardial sections (D), respectively. These histological analyses were further confirmed via transcriptional analysis of hypertrophy-related genes, which revealed a significant increase in *NPPB, MYH7*, and a decrease in *CCN2*, see Fig. 2C. Furthermore, we conducted a transcriptional analysis of fibrotic gene expression in RV free wall tissue, where *COL1A1, COL3A1, MMP2*, and *SDC1* transcription was significantly upregulated in PAH samples, while increases in *FN1* and *TGFB1* were also marginally increased, see Fig. 2D.

3.4. Pulmonary arterial hypertension led to disorganization of myocardial microstructure

Using DTI-MRI data, we computed the mean myocardial fiber orientation angles and divided the data into four equidistant sections (A-D) across the RV wall (similar to our histological analysis), see Fig. 3A. In contrast to our histological analysis, we performed the DTI-MRI tractography analysis for the entire RV, not just a mid-wall section. By fitting von Mises distributions to the diffusion tensor data, we could capture both the mean fiber angle and the extent of fiber splay or dispersion. Interestingly, we found that the mean fiber angle did not significantly change between PAH and CTL animals, see Fig. 3B. However, by comparing the concentration parameter b, see Eq. (1), between PAH and CTL animals, we found that myocardial fibers were more dispersed – i.e., less organized – in PAH animals than in CTL animals, see Fig. 3C. Recall that smaller b values imply a larger fiber dispersion.

3.5. Extracellular collagen deposition stiffened myocardium but is likely not the sole cause

From a comprehensive set of mechanical testing protocols, see Fig. 4A, B, we found that myocardial stiffness increased in PAH animals relative to CTL. Specifically, we found that the toe-region of samples significantly stiffened under shear, see Fig. 4C, D, and under extension and compression, see Fig. 4E, F. That is, myocardium showed stiffening under shear only at small strains ($p = 0.003$), while at large strains no statistical significance was found ($p = 0.161$), see also Supplementary Figure S3. In contrast, myocardium showed stiffening under extension and compression both at small strains ($p < 0.0001$) and large strains ($p = 0.015$). Interactions between disease and orientation were not significant. Thus, PAH-induced stiffening was not directionally dependent. Please see Supplementary Figure S4 for a comparison between the stress-strain curves of control and PAH tissue under all deformation modes. When correlating collagen content with each sample's stiffness in the circumferential direction (CC) we found a statistically significant ($p < 0.001$) and moderately strong relationship ($R^2 = 0.45$), see Fig. 4G, F. This may imply that increased collagen deposition in the PAH animals is, at least partially, responsible for the increased stiffness of the tissue; but not solely.

3.6. Myocardial stiffening is a significant if not primary cause for RV stiffening

Our data revealed three potential mechanisms of RV stiffening: i) thickened RV walls, ii) a disorganized microstructure, and iii) stiffened myocardium. To decouple these three mechanisms, we built finite element models of a simplified RV and used the models to simulate end-diastolic filling, see Fig. 5A. First, we only

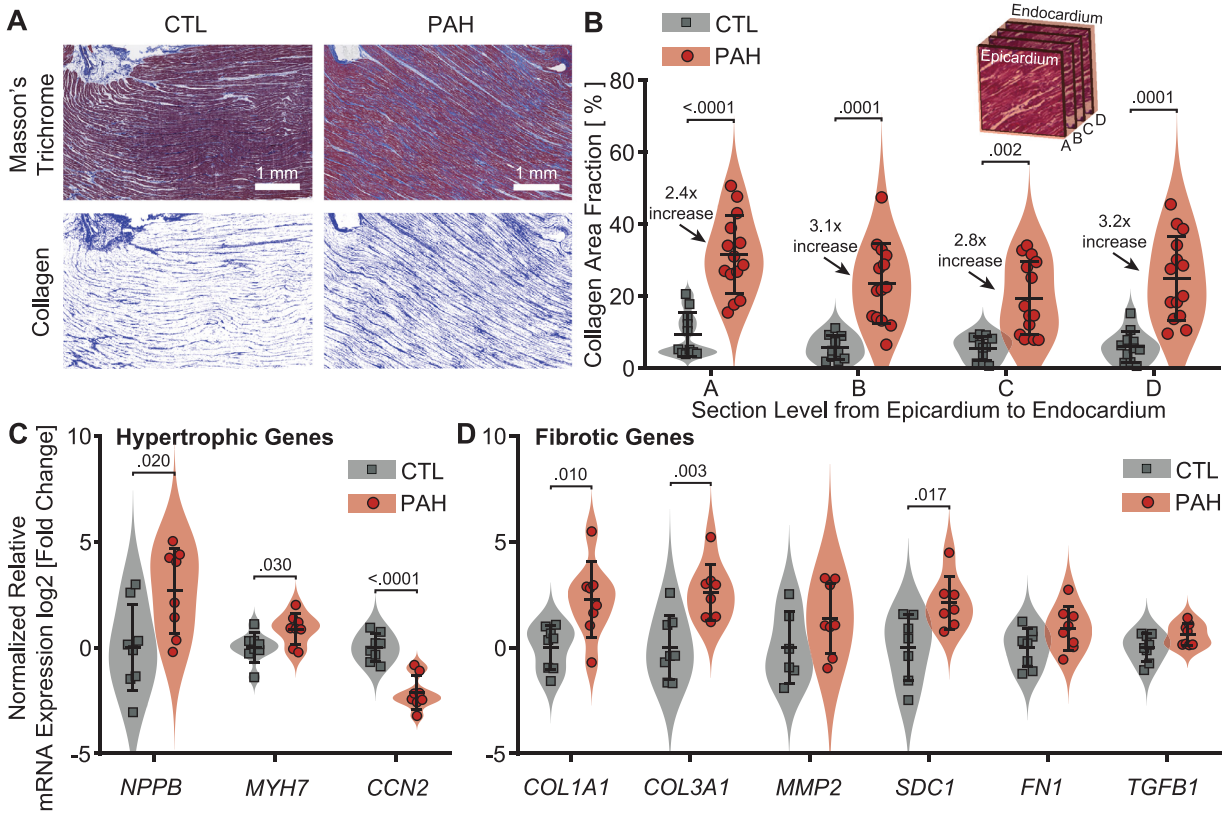

Fig. 2. Pulmonary arterial hypertension induced extracellular collagen synthesis.
A) Representative Masson's Trichrome stains of myocardium samples from control and pulmonary arterial hypertension (PAH) animals. B) Comparison of collagen area fractions in four sections across the myocardial free wall, between control (CTL, $n = 11$) and PAH ($n = 14$) specimens. Please note that discrepancies between subject numbers and specimen numbers stem from collecting multiple samples from some subjects. C) Relative expression of hypertrophy-related genes. D) Relative expression of fibrosis-related genes (CTL $n = 8$, PAH $n = 8$). Please note that discrepancies between subject numbers and specimen numbers stem from limited specimen availability and thus, some animals not being represented in the histology.

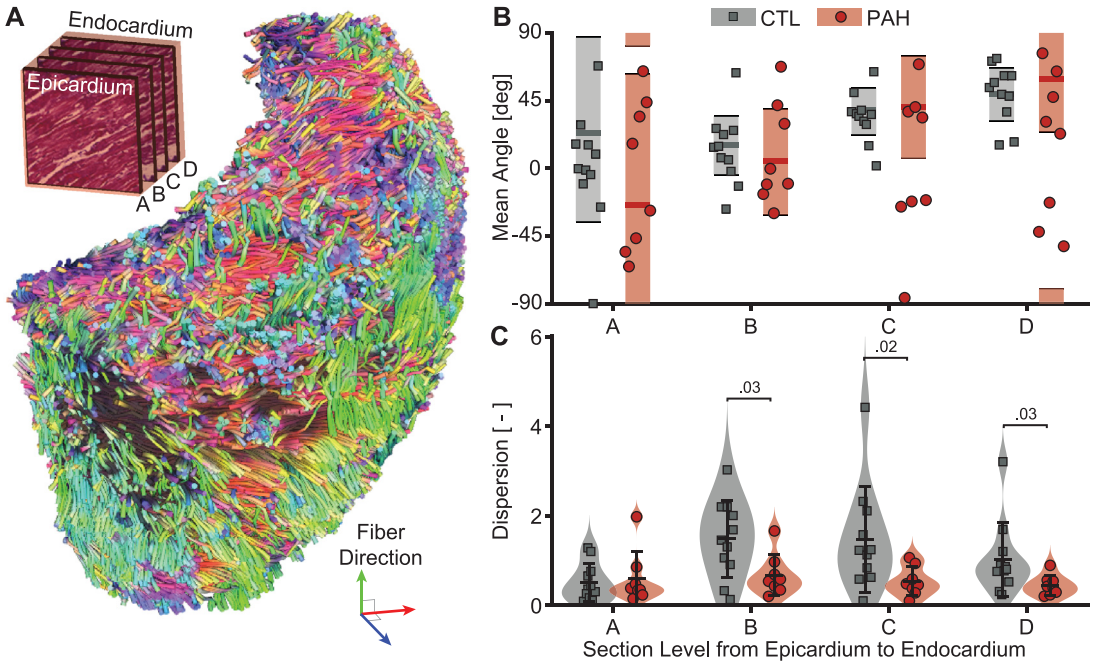

Fig. 3. Pulmonary arterial hypertension induced microstructural disorganization.
A) Representative diffusion tensor (DTI-MRI) tractography with orientation color coding. B) Mean fiber orientation angle in four sections across the right ventricular free wall. Shaded areas indicate the lower and upper bounds of the 95 % highest posterior density interval. C) Fiber dispersion in four sections across the right ventricular free wall. (control (CTL), $n = 11$; pulmonary arterial hypertension (PAH), $n = 8$). Please note that discrepancies between subject numbers and specimen numbers stem from some hearts not having undergone MRI imaging.

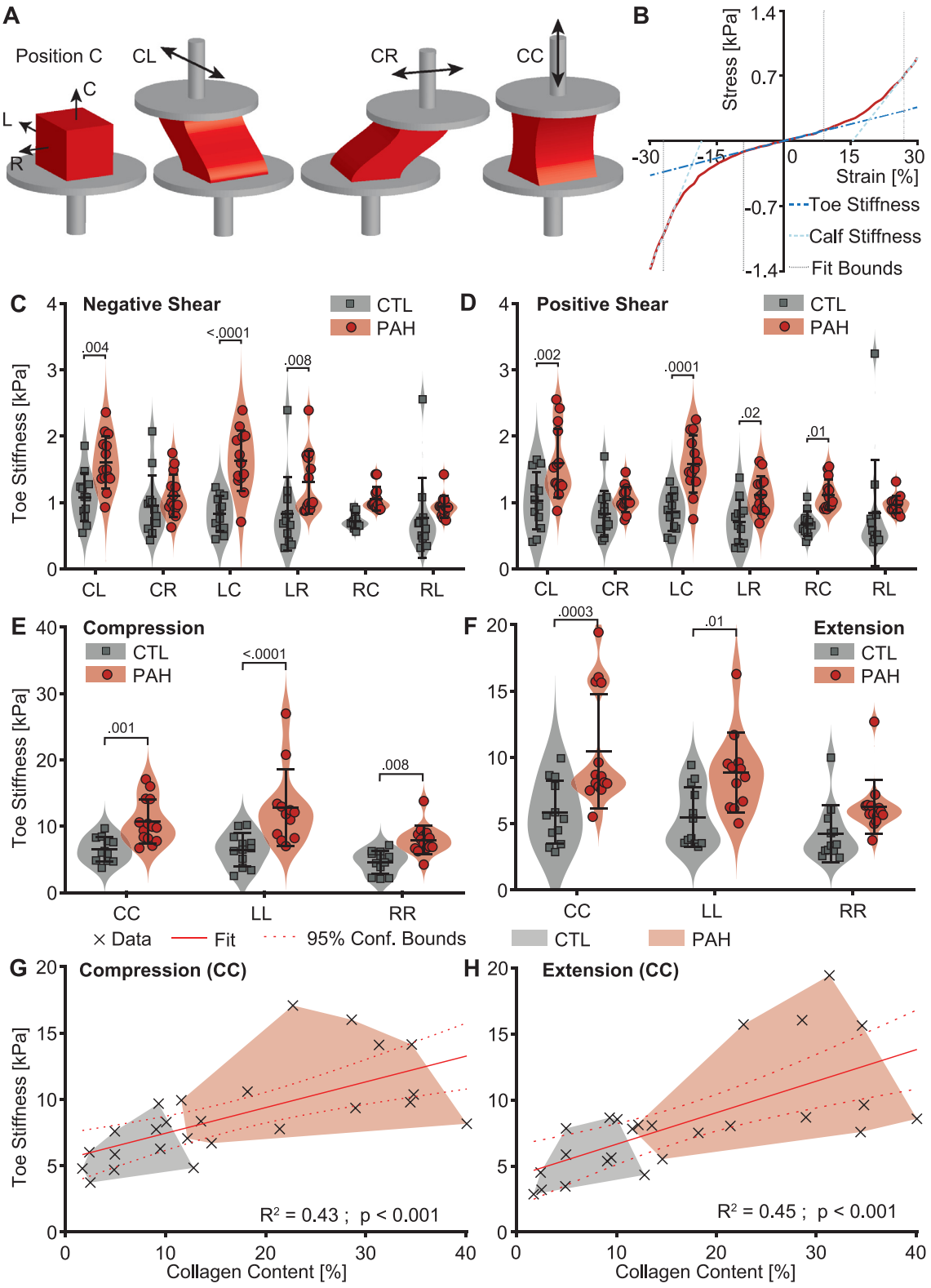

Fig. 4. Pulmonary arterial hypertension induced myocardial stiffening.
A) Nomenclature for mechanical testing modes, where C, L, and R are the circumferential, longitudinal, and radial shear directions. B) Representative stress-strain data. C-D) Toe stiffness (i.e., stiffness at small strains) in six shear directions in positive and negative directions. E-F) Toe stiffness under compression and tension in three material directions. (control (CTL), $n = 12$; pulmonary arterial hypertension (PAH), $n = 14$). G-H) Correlation between fiber compressive and tensile stiffness in the circumferential direction (CC) with collagen content (per area fractions) (CTL $n = 11$, PAH $n = 14$). Please note that discrepancies between subject numbers and specimen numbers stem from collecting multiple samples from some subjects.

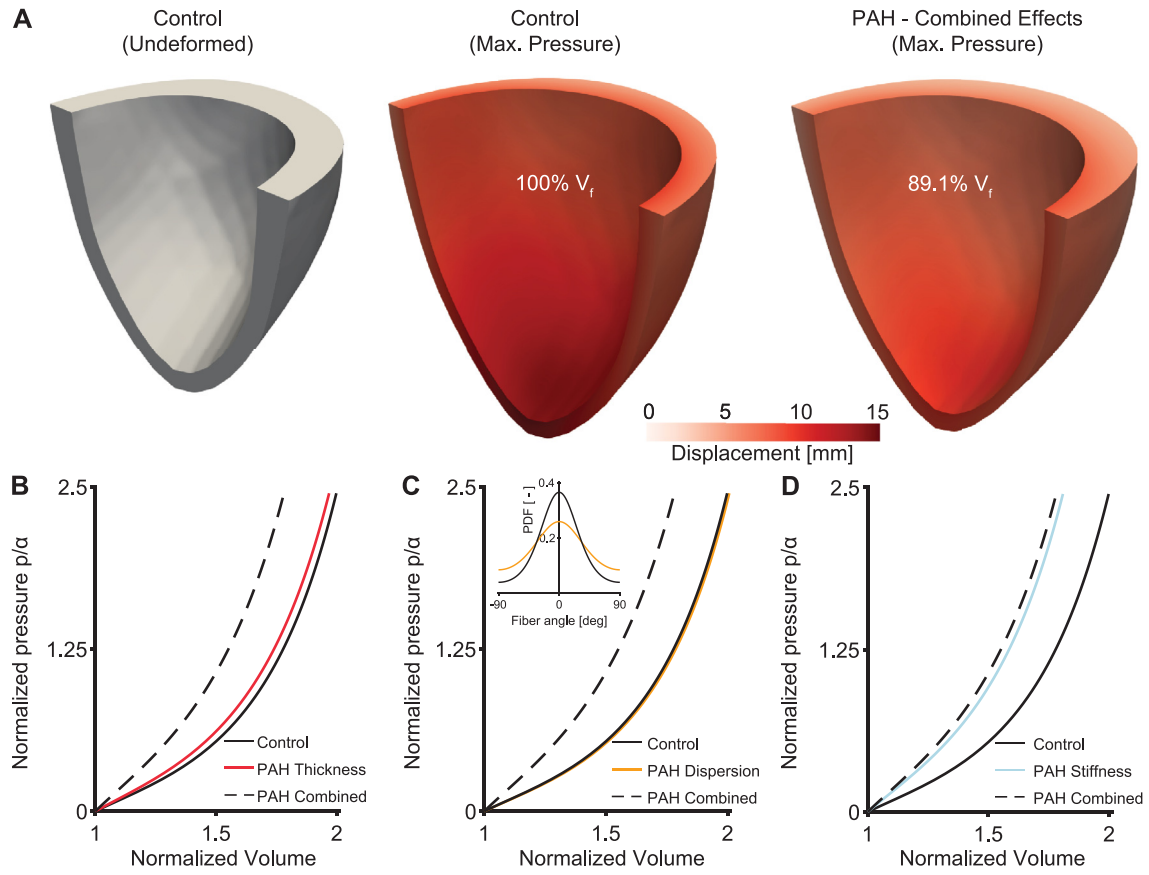

Fig. 5. Myocardial stiffness is the primary wall stiffening mechanism as predicted by a computational model of the right ventricle.
A) Simplified model of the right ventricle under zero pressure (gray) and at max pressure (red). We compared the diastolic filling volume (V_f) after accounting for pulmonary arterial hypertension (PAH)-induced changes in wall thickness, fiber dispersion myocardial stiffness, separately and combined. B-D) Passive filling curves of the right ventricle after wall thickening, changing fiber dispersion, and increasing myocardial stiffness, respectively, overlaid with the control case and the combined effects. Pressures (p) are normalized by the initial myocardial stiffness (a), while volumes are normalized by the pressure-free volume.

increased the wall thickness of our model according to our average PAH-induced findings, see Fig. 1C. This thickening induced only small changes in the passive filling curve, see Fig. 5B. In fact, at a normalized pressure of 2.5 (~40 mmHg) the total filling volume (V_f) decreased only by 1.5 %. Similarly, we drastically altered the myocardial organization and increased its fiber dispersion as seen in our PAH animals, see Fig. 5C. Again, we found only small effects on the passive filling curve with a marginally increased filling volume (V_f) of less than 0.5 %. Next, we increased the stiffness of our constitutive model reflecting the stiffness increases we observed in our PAH animals, see Fig. 5D. This change significantly altered the filling curve reducing V_f by 9.5 %; thus, significantly exceeding the effects of wall thickening and microstructural disorganization. Finally, we combined all three effects in our computational model. This lead to a decrease of V_f by 10.9 %, as shown by the dashed lines in all three curves in Fig. 5B-D.

4. Discussion

Our goal for this work was to use spatially- and directionally-sensitive measures of RV remodeling in a large animal model of PAH to delineate the relative importance of the different RV stiffening mechanisms of wall thickening, fiber orientation, and myocardial stiffness. This work provided new insights into the mechanisms of RV stiffening.

We confirmed that the RV adapts to hypertension via significant volumetric growth, primarily due to cardiomyocyte hypertrophy. Interestingly, this volumetric growth was not uniform. Instead, we found a markedly heterogeneous thickening. Specifically, the base and the free wall of the RV were thickened in the PAH animals, while the apex (e.g., markers 13 & 14 in Fig. 1C) and the wall near the interventricular septum (e.g., markers 6, 7, 10 & 11 in Fig. 1C) were nearly unchanged. This uneven distribution likely stems from differing growth stimuli across the wall, however, cardiomyocyte hypertrophy by WGA staining was only measured from mid-wall samples and thus not compared to similar measurements at the apex and septum. At the apex and the septum, where the RV is tied closely to the LV, mechanobiological stimuli are likely smaller than in the untied free wall and at the base [29]. This hypothesis agrees well with the general understanding that it is the lateral RV wall that dilates in RV failure and is implicated in tricuspid valve regurgitation [30]. Of note, others have made the opposite argument. Specifically, Andersen et al. concluded their meta-analysis on RV fibrosis with the observation that late gadolinium enhancement – as a measure of myocardial fibrosis – was found primarily near the RV insertion point at the interventricular septum and argued that higher local stresses may be the cause for those local hotspots [31]. Our contrasting findings imply that local hypertrophic thickening may not necessarily correlate with local fibrosis and that both phenomena should be viewed as separate stiffening mechanisms.

Regarding RV fibrosis, we confirmed that PAH induces significant collagen synthesis. Notably, we found an increase in interstitial collagen of more than 60 % in PAH tissue relative to CTL. This histological finding was consistent throughout the RV wall thickness and showed signs of persisting as several genes encoding fi-

brotic proteins continued to be upregulated in the myocardium at 8 weeks after pulmonary artery banding. This contrasts findings in humans where interstitial RV collagen accumulation has been described as minor [6,32]. One possible explanation for this difference in RV fibrosis across species is the fast onset of PAH in our animal model as opposed to the gradual onset of disease in (some) human conditions. It is possible that the fast adaptive response of the sheep RV may result in aberrant collagen synthesis as opposed to the more chronic natural history of human disease. This argument is supported by the findings of Rain et al., who observed that in rats with mild dysfunction, the RV stiffened primarily via hypertrophic thickening. However, in rats with severe RV dysfunction the ventricle stiffened primarily via myocardial stiffening as a result of collagen deposition [10]. Note that we evaluated collagen density as a measure of RV fibrosis only on mid-wall samples and thus cannot compare our findings to the reports based on late gadolinium enhancement-based spatial maps of fibrosis, as reported above.

When characterizing microstructural organization, we found that mean fiber directions across the RV had not changed, but that fiber dispersion had increased. DTI-MRI derived “fiber” orientation refers to the combined complex of cardiomyocytes and their extracellular matrix. Thus, we submit that increased fiber dispersion is likely a result of newly synthesized collagen being deposited into a pre-existing, pathologically deformed extracellular network and the associated dispersion of cardiomyocytes along their disorganizing extracellular matrix. However, these findings directly contrast with others’ prior studies in rodents that observed the opposite behavior – mean fiber direction was changed and fiber alignment increased [13,14]. The source of this disagreement is unknown and may be attributed to the difference between the natural history of RV remodeling in rodents and in our large animal model. That said, the current findings agree well with our prior work where we found tricuspid valve leaflets underwent the same fibrotic changes in animals with RV failure [33] and are consistent with a general understanding of microstructural remodeling associated with fibrosis [34].

Importantly, our large animal model of PAH confirmed several previous findings that PHT induces myocardial stiffening [10,13,35,36], although the current study is the first to subject maladapted RV myocardium to multi-directional shear loading scenarios. We found that RV myocardium had significantly stiffened in almost all shear directions. Additionally, myocardium stiffened under compression and tension in (nearly) all directions. At the same time, the measured stiffness increase in the circumferential direction correlated significantly with collagen content. Finally, we found that stiffness significantly differed only at small strains (i.e., toe stiffness), but not at large strains (i.e., calf stiffness). Recall, there are two broad contributors to myocardial stiffness: collagen-dominated extracellular stiffness and titin-dominated cellular stiffness [6]. The former depends on collagen type, cross-link density, collagen density, and collagen alignment [37–39]. The latter depends on titin isoform ratio and the state of titin phosphorylation [40]. Titin is activated even at small strains, while collagen is activated only at moderate to large strains [5,13]. Our observation that stiffness correlated moderately with collagen content implicates collagen as a significant contributor, but not the sole driver of myocardial stiffening. In addition, the dominance of small strain stiffening implicates titin as another possible important driver of stiffness. The absence of cell-level stiffness measurements in the current study, however, makes it difficult to draw detailed conclusions regarding the extent of titin-dependent intracellular myocardial stiffening mechanisms in our model of PAH.

Finally, we conducted a finite element analysis of RV diastolic filling and used this computational model to independently investigate the impact of each proposed stiffening mechanism – wall thickening, microstructural disorganization, and myocardial stiffening – on RV diastolic stiffness. Interestingly, we found that of the three mechanisms, myocardial stiffening had the largest influence. To ensure that our findings weren’t the result of poor modeling assumptions, we conducted sensitivity analyses and varied all elements of our model. That is, we tested different geometries, material models, and assumptions of the organization of the myocardium model. None of these numerical permutations fundamentally altered our findings. In support of our findings, Baicu et al. and Kwan et al. suggested that myocardial stiffening is an important adaptive mechanism that protects the RV from excessive dilation [18,36].

4.1. Clinical significance

The clinical significance of our work stems from several key points. First and foremost, we have demonstrated the immense remodeling potential of the RV in a large animal model. That is, after only 8 weeks of PAH the RV grew on average by 65 % in volume, remodeled its microstructure, and fundamentally altered its intrinsic material properties. Second, we showed that RV hypertrophy is driven primarily by growth at the base and free wall, while all other areas seem to be protected from excessive growth by the left ventricle. From a clinical perspective, this suggests RV hypertrophy should be evaluated with spatial heterogeneity in mind. That is, hypertrophy should be evaluated where the ventricle is likely most remodeled. Most importantly, our findings suggest that the inherent stiffness of the RV myocardium may be the primary driver of RV stiffening. Thus, myocardial stiffening via intracellular (titin activation) or extracellular mechanisms (collagen deposition) should be considered a prime candidate for predicting RV diastolic dysfunction. While there are global measures of RV stiffening, such as end-diastolic elastance, other direct and spatially-sensitive methods such as ultrasound- or MRI-based strain measurement techniques should be explored for the RV myocardium [41]. Finally, our work suggests that collagen synthesis and extracellular matrix fibrosis are critical drivers of myocardial stiffening of the RV. This is of potential clinical significance as modern MRI techniques are sensitive to collagen signatures and could be further used to non-invasively estimate material stiffness of the RV and to predict clinical outcomes of PHT and heart failure [42].

4.2. Limitations

The primary limitation of our study is that the onset of PAH in our animal model is sudden rather than progressive as in most clinical instances [43]. For example, others have found some evidence in rodents that suggests sudden onset PAH may have a different pathology than progressive onset PAH [18,36]. Future work with our large animal model of PAH will consider a progressive banding model as described by Ukita et al. [44] Additionally, we have captured only one time point at eight weeks of disease progression. Thereby, we are unable to characterize the temporal evolution of RV stiffening in this large animal model. We also did not conduct cell-level biophysical studies that could have provided further insight into the intracellular mechanisms of myocardial stiffening and potentially explain the relative importance of extracellular and intracellular contributions. Also, we are currently lacking quantitative models that allow a deeper insight into the functional importance of the highly orthotropic, mechanical response of the myocardium. Future modeling approaches paired with our data may provide valuable insight into these complex mechanics and allow for better clinical interpretation of our data. Finally, our study was conducted on sheep which may not fully resemble the human clinical condition.

5. Conclusion

We found that PAH induces RV wall thickening, microstructural disorganization, and myocardial stiffening. These mechanisms were both spatially and directionally dependent. Most critically, we observed – through experimental measures of fibrosis and numerical simulations of diastolic filling – that myocardial stiffening is the most important contributor to RV stiffening. Thus, by extension, myocardial stiffening may be an important predictor, if not the most important predictor, for PAH progression. Given the significant correlation between myocardial stiffening and collagen synthesis, extracellular matrix-sensitive imaging modalities may be used as a future clinical proxy for myocardial stiffness and a useful tool for evaluating disease outcomes.

Declaration of Competing Interest

The authors declare the following financial interests/personal relationships which may be considered as potential competing interests: Dr. Rausch has a speaking agreement with Edwards Lifesciences.

Acknowledgements

MKR acknowledges the partial support from the National Institutes of Health via grants R01HL165251 and R21HL161832, and the National Science Foundation via grant 2127925. TAT acknowledges the partial support from the National Institutes of Health via grants R01HL165251 and R21HL161832. MRB acknowledges support from the National Institutes of Health via grant R00HL146951. MM acknowledges support from the American Heart Association via its predoctoral fellowship 902502.

Supplementary materials

Supplementary material associated with this article can be found, in the online version, at doi:10.1016/j.actbio.2023.09.043.

References

[1] M. Humbert, O. Sitbon, A. Chaouat, M. Bertocchi, G. Habib, V. Gressin, A. Yaïci, E. Weitzenblum, J.-F. Cordier, F. Chabot, C. Dromer, C. Pison, M. Reynaud-Gaubert, A. Haloun, M. Laurent, E. Hachulla, V. Cottin, B. Degano, X. Jaïs, D. Montani, R. Souza, G. Simonneau, Survival in patients with idiopathic, familial, and anorexigen-associated pulmonary arterial hypertension in the modern management era, Circulation 122 (2) (2010) 156–163, doi:10.1161/CIRCULATIONAHA.109.911818.

[2] M.C. van de Veerdonk, T. Kind, J.T. Marcus, G.-J. Mauritz, M.W. Heymans, H.-J. Bogaard, A. Boonstra, K.M.J. Marques, N. Westerhof, A. Vonk-Noordegraaf, Progressive right ventricular dysfunction in patients with pulmonary arterial hypertension responding to therapy, J. Am. Coll. Cardiol. 58 (24) (2011) 2511–2519, doi:10.1016/j.jacc.2011.06.068.

[3] A.R. Tonelli, V. Arelli, O.A. Minai, J. Newman, N. Bair, G.A. Heresi, R.A. Dweik, Causes and circumstances of death in pulmonary arterial hypertension, Am. J. Respir. Crit. Care Med. 188 (3) (2013) 365–369, doi:10.1164/rccm.201209-1640OC.

[4] K. Tello, A. Dalmer, J. Axmann, R. Vanderpool, H.A. Ghofrani, R. Naeije, F. Roller, W. Seeger, N. Sommer, J. Wilhelm, H. Gall, M.J. Richter, Reserve of right ventricular-arterial coupling in the setting of chronic overload, Circ. Heart Fail. 12 (1) (2019) e005512, doi:10.1161/CIRCHEARTFAILURE.118.005512.

[5] S. Jang, R.R. Vanderpool, R. Avazmohammadi, E. Lapshin, T.N. Bachman, M. Sacks, M.A. Simon, Biomechanical and hemodynamic measures of right ventricular diastolic function: translating tissue biomechanics to clinical relevance, J. Am. Heart Assoc. 6 (9) (2017) e006084, doi:10.1161/JAHA.117.006084.

[6] S. Rain, M.L. Handoko, P. Trip, C.T.-J. Gan, N. Westerhof, G.J. Stienen, W.J. Paulus, C.A.C. Ottenheijm, J.T. Marcus, P. Dorfmüller, C. Guignabert, M. Humbert, P. MacDonald, C. dos Remedios, P.E. Postmus, C. Saripalli, C.G. Hidalgo, H.L. Granzier, A. Vonk-Noordegraaf, J. van der Velden, F.S. de Man, Right ventricular diastolic impairment in patients with pulmonary arterial hypertension, Circulation 128 (18) (2013) 2016–2025, doi:10.1161/CIRCULATIONAHA.113.001873.

[7] R.R. Vanderpool, M.R. Pinsky, R. Naeije, C. Deible, V. Kosaraju, C. Bunner, M.A. Mathier, J. Lacomis, H.C. Champion, M.A. Simon, RV-pulmonary arterial coupling predicts outcome in patients referred for pulmonary hypertension, Heart 101 (1) (2015) 37–43, doi:10.1136/heartjnl-2014-306142.

[8] P. Trip, S. Rain, M.L. Handoko, C. van der Bruggen, H.J. Bogaard, J.T. Marcus, A. Boonstra, N. Westerhof, A. Vonk-Noordegraaf, F.S. de Man, Clinical relevance of right ventricular diastolic stiffness in pulmonary hypertension, Eur. Respir. J. 45 (6) (2015) 1603–1612, doi:10.1183/09031936.00156714.

[9] B.S. Burlew, K.T. Weber, Cardiac fibrosis as a cause of diastolic dysfunction, Herz 27 (2) (2002) 92–98, doi:10.1007/s00059-002-2354-y.

[10] S. Rain, S. Andersen, A. Najafi, J. Gammelgaard Schultz, D. da Silva Gonçalves Bós, M.L. Handoko, H.-J. Bogaard, A. Vonk-Noordegraaf, A. Andersen, J. van der Velden, C.A.C. Ottenheijm, F.S. de Man, Right ventricular myocardial stiffness in experimental pulmonary arterial hypertension: relative contribution of fibrosis and myofibril stiffness, Circ. Heart Fail. 9 (7) (2016) e002636, doi:10.1161/CIRCHEARTFAILURE.115.002636.

[11] S. Rain, D. da S. G. Bos, M.L. Handoko, N. Westerhof, G. Stienen, C. Ottenheijm, M. Goebel, P. Dorfmüller, C. Guignabert, M. Humbert, H. Bogaard, C. dos Remedios, C. Saripalli, C.G. Hidalgo, H.L. Granzier, A. Vonk-Noordegraaf, J. van der Velden, F.S. de Man, Protein changes contributing to right ventricular cardiomyocyte diastolic dysfunction in pulmonary arterial hypertension, J. Am. Heart Assoc. 3 (3) (May 2014) e000716, doi:10.1161/JAHA.113.000716.

[12] K. Tello, A. Dalmer, R. Vanderpool, H.A. Ghofrani, R. Naeije, F. Roller, W. Seeger, J. Wilhelm, H. Gall, M.J. Richter, Cardiac magnetic resonance imaging-based right ventricular strain analysis for assessment of coupling and diastolic function in pulmonary hypertension, JACC Cardiovasc. Imaging 12 (11) (2019) 2155–2164, doi:10.1016/j.jcmg.2018.12.032.

[13] M.R. Hill, M.A. Simon, D. Valdez-Jasso, W. Zhang, H.C. Champion, M.S. Sacks, Structural and mechanical adaptations of right ventricle free wall myocardium to pressure overload, Ann. Biomed. Eng. 42 (12) (2014) 2451–2465, doi:10.1007/s10439-014-1096-3.

[14] R. Avazmohammadi, M. Hill, M. Simon, M. Sacks, Transmural remodeling of right ventricular myocardium in response to pulmonary arterial hypertension, APL Bioeng 1 (1) (2017) 016105, doi:10.1063/1.5011639.

[15] D. Valdez-Jasso, M.A. Simon, H.C. Champion, M.S. Sacks, A murine experimental model for the mechanical behaviour of viable right-ventricular myocardium: mechanical behaviour of viable right-ventricular myocardium, J. Physiol. 590 (18) (2012) 4571–4584, doi:10.1113/jphysiol.2012.233015.

[16] D. Vélez-Rendón, X. Zhang, J. Gerringer, D. Valdez-Jasso, Compensated right ventricular function of the onset of pulmonary hypertension in a rat model depends on chamber remodeling and contractile augmentation, Pulm. Circ. 8 (4) (2018) 1–13, doi:10.1177/2045894018800439.

[17] Y. Kusakari, T. Urashima, D. Shimura, E. Amemiya, G. Miyasaka, S. Yokota, Y. Fujimoto, T. Akaike, T. Inoue, S. Minamisawa, Impairment of excitation-contraction coupling in right ventricular hypertrophied muscle with fibrosis induced by pulmonary artery banding, PLoS ONE 12 (1) (2017) e0169564, doi:10.1371/journal.pone.0169564.

[18] C.F. Baicu, J. Li, Y. Zhang, H. Kasiganesan, G. Cooper, M.R. Zile, A.D. Bradshaw, Time course of right ventricular pressure-overload induced myocardial fibrosis: relationship to changes in fibroblast postsynthetic procollagen processing, Am. J. Physiol. 303 (9) (2012) H1128–H1134, doi:10.1152/ajpheart.00482.2012.

[19] T. Verbelen, D. Burkhoff, K. Kasama, M. Delcroix, F. Rega, B. Meyns, Systolic and diastolic unloading by mechanical support of the acute vs the chronic pressure overloaded right ventricle, J. Heart Lung Transplant. 36 (4) (2017) 457–465, doi:10.1016/j.healun.2016.10.003.

[20] S. Kakaletsis, W.D. Meador, M. Mathur, G.P. Sugerman, T. Jazwiec, M. Malinowski, E. Lejeune, T.A. Timek, M.K. Rausch, Right ventricular myocardial mechanics: multi-modal deformation, microstructure, modeling, and comparison to the left ventricle, Acta Biomater. 123 (2021) 154–166, doi:10.1016/j.actbio.2020.12.006.

[21] W.D. Meador, G.P. Sugerman, H.M. Story, A.W. Seifert, M.R. Bersi, A.B. Tepole, M.K. Rausch, The regional-dependent biaxial behavior of young and aged mouse skin: a detailed histomechanical characterization, residual strain analysis, and constitutive model, Acta Biomater. 101 (2020) 403–413, doi:10.1016/j.actbio.2019.10.020.

[22] W.D. Meador, M. Mathur, G.P. Sugerman, T. Jazwiec, M. Malinowski, M.R. Bersi, T.A. Timek, M.K. Rausch, A detailed mechanical and microstructural analysis of ovine tricuspid valve leaflets, Acta Biomater. 102 (2020) 100–113, doi:10.1016/j.actbio.2019.11.039.

[23] B. Emde, A. Heinen, A. Gödecke, K. Bottermann, Wheat germ agglutinin staining as a suitable method for detection and quantification of fibrosis in cardiac tissue after myocardial infarction, Eur. J. Histochem. (2014), doi:10.4081/ejh.2014.2448.

[24] T.D. Schmittgen, K.J. Livak, Analyzing real-time PCR data by the comparative CT method, Nat. Protoc. 3 (6) (2008) 1101–1108, doi:10.1038/nprot.2008.73.

[25] S.A. Maas, B.J. Ellis, G.A. Ateshian, J.A. Weiss, FEBio: finite elements for biomechanics, J. Biomech. Eng. 134 (1) (2012) 011005, doi:10.1115/1.4005694.

[26] J.C. Simo, R.L. Taylor, Quasi-incompressible finite elasticity in principal stretches. continuum basis and numerical algorithms, Comput. Methods Appl. Mech. Eng. 85 (3) (1991) 273–310, doi:10.1016/0045-7825(91)90100-K.

[27] J. Cremers, K.T. Mulder, I. Klugkist, Circular interpretation of regression coefficients, Br. J. Math. Stat. Psychol. 71 (1) (2018) 75–95, doi:10.1111/bmsp.12108.

[28] G. Nuñez-Antonio, E. Gutiérrez-Peña, A Bayesian model for longitudinal circular data based on the projected normal distribution, Comput. Stat. Data Anal. 71 (2014) 506–519, doi:10.1016/j.csda.2012.07.025.

[29] W.D. Meador, M. Malinowski, T. Jazwiec, M. Goehler, N. Quay, T.A. Timek, M.K. Rausch, A fiduciary marker-based framework to assess heterogeneity and anisotropy of right ventricular epicardial strains in the beating ovine heart, J. Biomech. 80 (2018) 179–185, doi:10.1016/j.jbiomech.2018.08.036.

[30] M.F. Dietz, E.A. Prihadi, P. van der Bijl, L. Goedemans, B.J.A. Mertens, E. Gursoy, O.S. van Genderen, N. Ajmone Marsan, V. Delgado, J.J. Bax, Prognostic implications of right ventricular remodeling and function in patients with significant secondary tricuspid regurgitation, Circulation 140 (10) (2019) 836–845, doi:10.1161/CIRCULATIONAHA.119.039630.
[31] S. Andersen, J.E. Nielsen-Kudsk, A. Vonk Noordegraaf, F.S. de Man, Right ventricular fibrosis: a pathophysiological factor in pulmonary hypertension? Circulation 139 (2) (2019) 269–285, doi:10.1161/CIRCULATIONAHA.118.035326.
[32] M.J. Overbeek, K.T.B. Mouchaers, H.M. Niessen, A.M. Hadi, K. Kupreishvili, A. Boonstra, A.E. Voskuyl, J.A.M. Belien, E.F. Smit, B.C. Dijkmans, A. Vonk-Noordegraaf, K. Grünberg, Characteristics of interstitial fibrosis and inflammatory cell infiltration in right ventricles of systemic sclerosis-associated pulmonary arterial hypertension, Int. J. Rheumatol. 2010 (2010) 1–10, doi:10.1155/2010/604615.
[33] W.D. Meador, M. Mathur, G.P. Sugerman, M. Malinowski, T. Jazwiec, X. Wang, C.M. Lacerda, T.A. Timek, M.K. Rausch, The tricuspid valve also maladapts as shown in sheep with biventricular heart failure, Elife 9 (2020) e63855, doi:10.7554/eLife.63855.
[34] S. Ricard-Blum, G. Baffet, N. Théret, Molecular and tissue alterations of collagens in fibrosis, Matrix Biol 68–69 (2018) 122–149, doi:10.1016/j.matbio.2018.02.004.
[35] D. Vélez-Rendón, E.R. Pursell, J. Shieh, D. Valdez-Jasso, Relative contributions of matrix and myocytes to biaxial mechanics of the right ventricle in pulmonary arterial hypertension, J. Biomech. Eng. 141 (9) (2019) 091011, doi:10.1115/1.4044225.
[36] E.D. Kwan, D. Vélez-Rendón, X. Zhang, H. Mu, M. Patel, E. Pursell, J. Stowe, D. Valdez-Jasso, Distinct time courses and mechanics of right ventricular hypertrophy and diastolic stiffening in a male rat model of pulmonary arterial hypertension, Am. J. Physiol. 321 (4) (2021) H702–H715, doi:10.1152/ajpheart.00046.2021.
[37] D. Chapman, K.T. Weber, M. Eghbali, Regulation of fibrillar collagen types I and III and basement membrane type IV collagen gene expression in pressure overloaded rat myocardium, Circ. Res. 67 (4) (1990) 787–794, doi:10.1161/01.RES.67.4.787.
[38] K.T. Weber, Cardiac interstitium in health and disease: the fibrillar collagen network, J. Am. Coll. Cardiol. 13 (7) (1989) 1637–1652, doi:10.1016/0735-1097(89)90360-4.
[39] J.P.M. Cleutjens, M.J.A. Verluyten, and J.F.M. Smits, “Collagen remodeling after myocardial infarction in the rat heart,” vol. 147, no. 2, 1995.
[40] M.M. LeWinter, H. Granzier, Cardiac titin: a multifunctional giant, Circulation 121 (19) (May 2010) 2137–2145, doi:10.1161/CIRCULATIONAHA.109.860171.
[41] C.C. Earl, F.W. Damen, M. Yin, K.L. Aasa, S.K. Burris, C.J. Goergen, Strain estimation of the murine right ventricle using high-frequency speckle-tracking ultrasound, Ultrasound Med. Biol. 47 (11) (2021) 3291–3300, doi:10.1016/j.ultrasmedbio.2021.07.001.
[42] Y. Dong, Z. Pan, D. Wang, J. Lv, J. Fang, R. Xu, J. Ding, X. Cui, X. Xie, X. Wang, Y. Chen, X. Guo, Prognostic value of cardiac magnetic resonance–derived right ventricular remodeling parameters in pulmonary hypertension: a systematic review and meta-analysis, Circ. Cardiovasc. Imaging 13 (7) (2020) e010568, doi:10.1161/CIRCIMAGING.120.010568.
[43] R.T. Schermuly, H.A. Ghofrani, M.R. Wilkins, F. Grimminger, Mechanisms of disease: pulmonary arterial hypertension, Nat. Rev. Cardiol. 8 (8) (2011) 443–455, doi:10.1038/nrcardio.2011.87.
[44] R. Ukita, J.W. Stokes, W.K. Wu, J. Talackine, N. Cardwell, Y. Patel, C. Benson, C.T. Demarest, E.B. Rosenzweig, K. Cook, E.J. Tsai, M. Bacchetta, A large animal model for pulmonary hypertension and right ventricular failure: left pulmonary artery ligation and progressive main pulmonary artery banding in sheep, J. Vis. Exp. (173) (2021) 62694, doi:10.3791/62694.